Noname manuscript No.
(will be inserted by the editor)

Non-visible Transformations of Chaotic Attractors due to their Ultra Low Density in AC-DC Power Factor Correction Converters

Viktor Avrutin · Zhanybai T. Zhusubaliyev · Abdelali El Aroudi

the date of receipt and acceptance should be inserted later

Abstract It is well known that models of power electronic converters belong to the scope of the theory of piecewise smooth systems. Recently, it has been shown that DC-AC and AC-DC power converters (whose dynamics is governed by two vastly different frequencies) lead to a special class of piecewise smooth models whose properties have been barely investigated before. The characteristic feature of these models is a very high (practically unpredictable) number of switching manifolds between partitions in the state space associated with different dynamics. In the previous publications we have considered several models of DC-AC converters and have shown that the properties of their models lead to a number of unusual dynamic phenomena. In particular, we have shown that transformations of chaotic attractors in such models can be caused in the regions of the attractors associated with an ultra low invariant density, which is beyond a practical observability in physical or numerical experiments. The appearance of such low-density regions has been explained by the so-called spiking phenomenon. In the present paper, we make the next step and ask the natural question what are the reasons behind the appearance of spikes. We consider a model of a power converter belonging to a different class than the models considered before (a PFC AC-DC converter) and discuss a connection between spiking and the presence of two vastly different frequencies in the modeled system. This leads us to the conclusion that the described properties of transformations of chaotic attractors are generic for a broad class of power converters.

Keywords power electronic AC-DC PFC converter · piecewise-smooth map · chaotic attractor · homoclinic bifurcation

1 Introduction

Power electronics converters are used in many industrial applications such as in motor drives [1], interfaces between the renewable energy resources and loads [2], electrical vehicle battery charging [3], efficient emerging Light Emitting Diode (LED) lighting [4] among others. Their control is based on adequate switching between different circuit topologies using active and passive switching devices. The standard technique for driving the active switching devices is by means of a fixed frequency pulse width modulation (PWM). Accordingly, as any other switching circuits, power converters belong to the scope of the theory of piecewise smooth systems [5,6].

Many modern loads for the electrical mains are are nonlinear and this can induce serious power quality problems. With the increasing demand for power from the AC line and more constraints for

Viktor Avrutin (corresponding author)
Institute for Systems Theory and Automatic Control, University of Stuttgart, Pfaffenwaldring 9, 70550 Stuttgart, Germany; E-mail: avrutin@ist.uni-stuttgart.de

Zhanybai T. Zhusubaliyev
Department of Computer Science, Southwest State University, 50 Years of October Str. 94, 305040, Kursk, Russia; E-mail: zhanybai@hotmail.com

Abdelali El Aroudi
University Rovira i Virgili; Departament d'Enginyeria Electronica, Av. Paisos Catalans, no. 27, 43007, Tarragona, Spain; E-mail: abdelali.elaroudi@urv.cat

power quality, including a Power Factor Correction (PFC) circuit is necessary to comply with the regulatory requirements and standards such as the IEC61000-3-2. Basically, A PFC circuit is an AC-DC converter usually controlled by pulse width modulation strategy and input current control. This control is performed in such a way to maximize the active power extracted from the available mains and in this way, the converter emulates a pure resistance. Therefore, the extracted current from the mains is in phase with the mains voltage hence resulting in a unity power factor hence minimizing waste of electrical energy and improving the system efficiency. A diode rectifier followed by a boost converter working in Continuous Conduction Mode (CCM) is the most popular unidirectional AC-DC converter commonly used for many medium and high power applications [7,8].

For an appropriate functioning of this system, the output voltage of the boost converter must be always higher than the peak line voltage. For usual line input voltage applications, the bus voltage is usually fixed to values around 380 V DC which is achieved by a voltage feedback compensating loop. One of the important tasks in the design of PFC power supplies is the control loop implementation which ensures a system free from any kind of instabilities, with an adequate dynamic behavior under all loading and power conditions. However, it is well known that this aim is difficult to be achieved for all values of system parameters. A series of studies dealing with nonlinear behavior in these systems have been carried out in the past [9–11]. Later, many studies have dealt with such effects occurring in boost PFC circuits as the period doubling instability at the line frequency, as well as the appearance of bubbling at the switching frequency (often, although not entirely correctly, referred to as the fast-scale period doubling) [12–15]. Understanding of these phenomena is extremely important for design, prediction and control of the dynamics occurring in this type of power electronics systems.

The major part of the results on possible bifurcation phenomena in several classes of switching power converters have been achieved for DC-DC converters, in particular because the converter of this class leads to relatively simple models [16–18,5,19,6,20]. By contrast to that, converters of the DC-AC and AC-DC types are more difficult to deal with, since their dynamics is governed by two vastly different frequencies, namely the high switching frequency and the low line frequency which may be related to the output (DC-AC) or input (AC-DC) signals. The ratio m between these frequencies is referred to as the *frequency modulation ratio*, and takes typically the values of the magnitude between 10^2 and 10^3.

In our previous publications [21–23] we presented a generic two-step approach for modeling of power converters.

- The first step of this approach is common to all classes of converters and involves the calculation of a *primary stroboscopic mapping* with the sampling frequency equal to the high switching frequency. For DC-DC converters the resulting stroboscopic map is in general autonomous and represents already a final model, while for DC-AC and AC-DC such a primary stroboscopic map depends on the phase of the low frequency signal, i.e., is non-autonomous.
- As a second step, specific for DC-AC and AC-DC converters, we introduce a *secondary stroboscopic mapping* with the sampling frequency equal to the low frequency. Provided that the frequency modulation ratio is an integer number, the secondary stroboscopic map can be obtained from the iterate of the primary stroboscopic map which corresponds to one period of the low frequency signal (for example, the m-th iterate in the case of the DC-AC converters considered in the works cited above). Moreover, since the sampling frequency is chosen to be identical with the low frequency, the secondary stroboscopic map is autonomous.

Due to a high value of m, the resulting model (the secondary stroboscopic map) belongs to a specific class of piecewise smooth maps barely investigated before. The characteristic feature of maps belonging to this class is *an extremely high number of the switching manifolds* separating the branches of the function which governs the dynamics. This can easily be understood, taking into account that for any piecewise smooth map the number of branches of the m-th iterate grows exponentially with m.

Clearly, the presence of an extremely high number of branches essentially influences the dynamics and causes several unusual phenomena to occur, as for example transitions to chaos via irregular cascades of border collisions [21], structures in parameter space formed by persistence border collisions inside the domain of regular dynamics [22], and a global alignment of the boundaries associated with smooth bifurcations [23].

Transformations of chaotic attractors in a map with an extremely high number of branches resulting from the modeling of a DC-AC converter have been considered recently in [24]. In the cited work we have shown that transformations of chaotic attractors in this map can be explained by well known homoclinic bifurcations, which however, in addition to their usual effects, lead to the appearance of the regions of chaotic attractors associated with a very low invariant density. In many cases, this density is below the observability level, both in physical and numerical experiments based on forward iterations of the models. In the cited work, we explained the presence of these low density regions by the so-called spiking effect, i.e., the appearance of a small number of branches of the map with very small domains and unusually large ranges. However, in [24], the natural question "what are the reasons for the spiking phenomenon to occur?" has been left out for the future research.

In fact, quite unusual transformations of chaotic attractors in an AC-DC converter model has been reported for the first time in [25], but not explained. In the present work, we turn back to the model considered in that publication. Applying to this model the two-step approach recently developed for DC-AC converters and considering the secondary stroboscopic mapping, we can explain these phenomena. Following the line of research started in [24], in the present work we aim to demonstrate that spiking and similar effects influence transformations of chaotic attractors in models of AC-DC converters in a way similar to the one already reported for models of DC-AC converters. However, the main goal of the present work is to identify the sources of the spiking phenomenon. To this end we introduced a novel approach, similar to the usual cobweb diagrams but applicable to non-autonomous 1D maps. Using this approach we demonstrate that the appearance of spikes under parameter variation is caused by a change of the positions of some specific images of the border points of the function with respect to each other. As a next step, we provide some evidence in which class of models this phenomenon occurs. Although this question can still not be seen as completely solved, we present some evidence that spiking is caused by the presence of two different frequencies governing the dynamics and is therefore a generic phenomenon in DC-AC and AC-DC converters.

The paper is organized as follows. First, in Sect. 2 we briefly describe the investigated circuit and its discrete-time models (the primary and the secondary stroboscopic maps). Then, in Sect. 3 we discuss several transformations of chaotic attractors in the considered model, the spiking-related mechanisms leading to their appearance, and the connection of the observed effects to the low density parts of chaotic attractors. The mechanism causing the spikes to emerge is discussed in Sect. 4. Thereafter, in Sect. 5, we turn to the question which properties of the considered model lead to the spiking phenomenon. Sect. 6 concludes.

2 Modeling

2.1 System description

The block diagram of a typical AC-DC boost rectifier for PFC is shown in Fig. 1. The supply voltage (AC 50 − 60 Hz) at the system input is first applied to a diode full wave bridge rectifier to obtain a full wave rectified voltage $v_g(t)$ whose frequency is doubled (100−120 Hz). Then, this voltage is supplied to a current-mode controlled DC-DC boost converter whose main task is to perform the correction of the input PF.

In practice, at the output side of this converter, there is a large capacitor C to provide a roughly DC voltage V_0 from the AC voltage source $v_g(t)$ with relatively small ripple. Usually, the voltage controller consists of a feedback compensating loop, and the average output voltage V_0 is roughly regulated to a value between 380 V and 400 V DC for a line input voltage between 85 V AC and 265 V AC.

In order to generate the switching signal to the DC-DC boost converter, the feedback corrector first determines the error signal $\xi = V_{\mathrm{ref}}(t) - V_{\mathrm{cs}}(t)$ that measures the difference between the reference voltage $V_{\mathrm{ref}}(t)$ and the output voltage $V_{\mathrm{cs}}(t) = \vartheta i_L(t)$ of the current sensor (CS). Here, i_L is the inductor current and ϑ is referred to as the current sensor sensitivity parameter.

To ensure that the average value of the inductor current i_L is in phase with the input voltage, the reference signal V_{ref} is given by the rectified voltage $v_g(t)$ multiplied by a suitable transfer coefficient g:

$$V_{\mathrm{ref}}(t) = g\, v_g(t).$$

Here, the coefficient g is provided by the slow output of the external voltage controller VC and $v_g(t) = V_g|\sin(\omega_l t)|$ is the rectified sinusoidal voltage with the amplitude V_g and the angular frequency $\omega_l = 2\pi/T_\ell$. Hence,

$$V_{\mathrm{ref}}(t) = g\, V_g|\sin(\omega_l t)|.$$

As mentioned before, the value of the transfer coefficient g is given by a low bandwidth external loop controller regulating the output voltage. In most applications, this coefficient as well as the output voltage V_0 can be considered as constant.

The sample-and-hold unit S/H reads the error signal $\xi(t)$ at every clock time $t = kT$, $0, 1, 2, \ldots$ and maintains it for the following switching period. This produces the control signal $V_{\mathrm{con}}(t)$. Then, the comparator DA compares this signal with a periodic ramp function $V_{\mathrm{ramp}}(t)$ in order to generate the switching signals to the switch S.

The ramp function $V_{\mathrm{ramp}}(t)$ varies from zero to $-I_0$ in synchrony with the clock signal V_{clock}. If $V_{\mathrm{con}}(t) > 0$ or $V_{\mathrm{con}}(t) < -I_0$, the modulator is saturated. In the first case, i.e., if $V_{\mathrm{con}}(t) > 0$, the duration of the pulse is equal to the ramp period T, and in the second case (i.e., if $V_{\mathrm{con}}(t) < -I_0$) it is equal to zero.

In this way, the dynamics of PFC converters are characterized by two forcing frequencies: the switching frequency $f_s = 1/T$ and the line frequency $f_\ell = 1/T_\ell$ with $f_\ell \ll f_s$, where T_ℓ is the period of the reference signal and T is the ramp period (the period of the clock signal).

2.2 Model in continuous time

The dynamics of a PFC converter described above can be represented by the following non-autonomous differential equation with a discontinuous right hand side:

$$L\frac{di_L}{dt} = \begin{cases} V_g|\sin(\omega_l t)|, & \text{if } V_{\mathrm{con}} > V_{\mathrm{ramp}}(t), \\ V_g|\sin(\omega_l t)| - V_0, & \text{if } V_{\mathrm{con}} < V_{\mathrm{ramp}}(t), \end{cases}$$

with

$$\begin{aligned} V_{\mathrm{con}} &= \xi(t)|_{t=kT}\,, \\ \xi(t) &= g\,V_g|\sin(\omega_l t)| - \vartheta\, i_L(t), \\ V_{\mathrm{ramp}}(t) &= -I_0\left(1 - \frac{t}{T} + \left\lfloor \frac{t}{T} \right\rfloor\right), \\ \omega_l &= \frac{2\pi}{mT},\ \frac{T_\ell}{T} = m, \end{aligned}$$

where number $\lfloor t/T \rfloor$ is the largest integer number not greater than t/T (i.e., the integer part, or floor, of t/T) and, as previously introduced, m is referred to as the frequency modulation ratio, i.e., the number of clock cycles during the period T_ℓ of the reference signal.

Let us introduce now the dimensionless state variable $x = \dfrac{L\omega_l}{V_0} \cdot i_L$, the dimensionless time variable $\tau = \omega_l t$ and the following set of dimensionless parameters:

$$P = \frac{I_* L\omega_l}{\vartheta V_0},\ \varGamma = \frac{I_0}{I_*},\ \beta = \frac{gV_g}{\vartheta V_0}L\omega_l,\ \gamma = \frac{V_g}{V_0}.$$

The parameters P and $\varGamma$ control the amplitude of the ramp function normalized with respect to $I_* = 1$ A, β represents the amplitude of the AC line voltage, and γ is the normalized amplitude of the rectified sinusoidal source voltage. For simplicity, m is assumed to be an odd integer.

In these terms, the behavior of the considered converter is described by the following ordinary differential equation with a discontinuous right-hand side:

$$\dot{x} = \begin{cases} \gamma\,|\sin\tau|, & \text{if } \varphi(\tau, x) > 0; \\ \gamma\,|\sin\tau| - 1, & \text{if } \varphi(\tau, x) < 0, \end{cases} \tag{1}$$

where $\dot{x}$ denotes the derivative of x with respect to τ. The scalar function $\varphi(\tau, x)$

$$\varphi(\tau, x) = \ x_k - \beta\left|\sin\left(\frac{2\pi k}{m}\right)\right| - \eta(\tau),$$

with

$$\begin{aligned} &\eta(\tau) = P\,\varGamma\left(1 - \frac{m}{2\pi}\,\tau + \left\lfloor \frac{m}{2\pi}\,\tau \right\rfloor\right), \\ &\left\lfloor \frac{m}{2\pi}\,\tau \right\rfloor = k, \quad x_k = x(k) = x\left(\left\lfloor \frac{m}{2\pi}\,\tau \right\rfloor\right) \end{aligned}$$

defines the switching manifold (sometimes referred to as the discontinuity boundary)

$$\varSigma = \{(\tau, x) \mid \varphi(\tau, x) = 0\}.$$

The manifold $\varSigma$ separates the phase space of Eq. (1) in two partitions

$$\Big\{(\tau, x) \mid \varphi(\tau, x) > 0\Big\} \quad \text{and} \quad \Big\{(\tau, x) \mid \varphi(\tau, x) < 0\Big\}$$

in which the dynamic behavior of the system is governed by different vector fields. As shown in our recent publications [21–23], all solutions to Eq. (1) intersect the switching manifold $\varSigma$ transversely so that no sliding motion can occur.

2.3 Primary stroboscopic mapping

The derivation of the discrete-time model of the circuit described above is presented in [25]. This model (the primary stroboscopic mapping) is obtained by integration of the continuous time model over one ramp period and, in the normalized form (with the dimensionless state variable and parameters), is given by

$$x_{k+1} = F_k(x_k), \tag{2a}$$

where

$$F_k(x_k) = \begin{cases} F_k^{\mathcal{L}}(x_k) = x_k + \alpha \cdot \sin\left(\pi \dfrac{2k+1}{m}\right) \\ \qquad\qquad \text{if } x_k < b_k^-; \\ F_k^{\mathcal{M}}(x_k) = x_k + \alpha \cdot \sin\left(\pi \dfrac{2k+1}{m}\right) - \dfrac{2\pi}{m} z_k \\ \qquad\qquad \text{if } b_k^- \leqslant x_k \leqslant b_k^+; \\ F_k^{\mathcal{R}}(x_k) = x_k + \alpha \cdot \sin\left(\pi \dfrac{2k+1}{m}\right) - \dfrac{2\pi}{m} \\ \qquad\qquad \text{if } x_k > b_k^+ \cdot \mathit{\Gamma}, \end{cases} \tag{2b}$$

with

$$z_k = \frac{|q_k - x_k|}{P \cdot \mathit{\Gamma}} \ , \tag{2c}$$

$$q_k = \beta \sin\left(2\pi \frac{k}{m}\right), \ \ \alpha = 2\,\gamma \sin\left(\frac{\pi}{m}\right), \tag{2d}$$

$$b_k^- = q_k, \ \ b_k^+ = q_k + P \cdot \mathit{\Gamma}. \tag{2e}$$

The shape of the function $F_k(x)$ for $0 \leqslant k < \frac{1}{2}m$ is shown in Fig. 2. It follows from Eqs. (2b), (2c) and (2d) that the function $F_k(x)$ is $\frac{1}{2}m$-periodic with respect to k.[1]

As in [25], let us fix the following parameter values: $g = 0.01$; $V_g = 220\sqrt{2}$ V; $V_0 = 380$ V, $L =$ 15 mH; $I_* = 1$ A, $T_\ell = 1/f_\ell = 20$ ms, $\vartheta = 1.0\ \mathit{\Omega}$ and consider $\mathit{\Gamma}$ as a control parameter.

2.4 Secondary stroboscopic mapping

The bifurcation diagram of map (2) obtained at the previous parameter values which correspond to the results reported in [25] are shown in Fig. 3(a). Up to some extent this bifurcation diagram resembles the well know bandcount doubling cascade which is typical for piecewise smooth maps as for example the skew tent map [26,27]. Recall that this scenario represents a sequence parameter intervals corresponding to 2^k-band chaotic attractors, $k \geqslant 0$, separated from each other by the points of merging bifurcations [28,27] associated with homoclinic bifurcations of harmonic 2^k-cycles [29,26]. Still, there are several features in the bifurcation diagram shown in Fig. 3(a) which does not match the properties of the bandcount doubling cascade. The most striking of them are parameter intervals associated with missing bands of the attractors which interrupt the scenario repeatedly but without any recognizable systematics. Moreover, in some parts of the bifurcation diagram the chaotic attractors contain regions associated with extremely low density (which have been overseen in [25] and wrongly interpreted as gaps between the bands of multi-band chaotic attractors). Finally, in some parameter intervals the scenario is enriched by bistability, as indicated in Fig. 3(a).

All the phenomena mentioned above indicate clearly that the observed sequence of bifurcations differs from the bandcount doubling scenario and requires an explanation. To this end, one can make use of the technique recently developed for models of DC-AC converters and successfully applied in [21–23]. Proceeding in this way, one considers a secondary stroboscopic mapping over one period of the low frequency signal. Indeed, since the dynamics of the PFC AC-DC converter discussed in the present work is essentially governed by two frequencies, the primary stroboscopic mapping (2) over one period of the fast switching signal is non-autonomous. However, as the function $F_k(x)$ is $\frac{1}{2}m$-periodic with respect to k, the secondary stroboscopic mapping over one period of the low frequency signal is given by the $\frac{1}{2}m$-th iterate of the primary stroboscopic mapping. Moreover, for the same reason, for each value of i such that $0 \leqslant i < \frac{1}{2}m$, the corresponding iterate function

$$\begin{aligned} x_{k+1} = & f^{m/2}(x_k) = F_{k+i+\frac{1}{2}m-1} \circ \\ & F_{k+i+\frac{1}{2}m-2} \circ \cdots \circ F_{k+i+1} \circ F_{k+i}(x_k) \end{aligned} \tag{3}$$

is autonomous. The results presented in [21–23] confirm that several dynamical effects in power converters whose dynamics is governed by two vastly different frequencies are easier to investigate using 1D autonomous maps similar to (3) (for which the desired behavior of the converter corresponds to a stable fixed point) than using non-autonomous maps similar to (2). However, the price to pay for this explication is the necessity to work with a high iterate. Indeed, in the present case, the values of the parameters $T_\ell = 20$ ms; $T = 200\ \mu$s used in [25] lead to the frequency modulation ratio $m = 1000$, so that one has to consider the function f^{500}. As a matter of fact, a numerical treatment of this function is related to serious problems. Since the particular parameter values are of minor significance for the purposes of this paper, we prefer to avoid these problems and to change the param-

---

[1] Note that the function $F_k(x)$ has two arguments, x and k (see Fig. 2). For sake of compactness, we use a mixed notation and write the second argument as a lower index.

eters to the values $T_\ell = 1$ ms; $T = 50$ μs, which lead to the frequency modulation ratio $m = 200$. Proceeding in this way one has to consider the iterate function f^{100} (as in [21–23]). The bifurcation diagram obtained in this case is shown in Fig 3(b). Clearly, the overall shape of the bifurcation diagram changes significantly compared with the one shown in Fig 3(a). However, the mechanism causing the transformations of chaotic attractors remains the same and can be investigated more easily in the case of f^{100} than in the case of f^{500}. Specifically, in the following we consider the part of the bifurcation diagram which is shown outlined by a rectangle R_1 in Fig 3(b) and magnified in Fig 3(c). As shown below, in this part one can clearly observe several mechanisms leading to transformations of chaotic attractors due to the spiking phenomenon and similar effects.

3 Transformations of chaotic attractors and low density chaos

Let us start with the part of the bifurcation sequence outlined by the rectangle marked by R_2 in Fig 3(c) and shown magnified in Fig 3(d). In the left part of the bifurcation diagram the map has two coexisting attractors. First, for increasing value of Γ, the attractors do not undergo any visible changes, then at some parameter value the lower attractor start to shrink in size. Thereafter it keeps its smaller size for some parameter interval, and eventually it grows back to its previous size. Eventually, the upper attractor starts to grow (note that the density in the added part of the attractor is much lower than in the other part) and then it disappears, leaving only the lower attractor to exist in the right part of the bifurcation diagram.

To explain the observed transformations of the attractors let us consider the shape of the function $f^{m/2}$ at some characteristic parameter values. The function $f^{m/2}$ at the parameter values corresponding to the point A_1 in Fig 3(d) is shown in Fig. 4(a). In is clearly visible in this figure that at the considered parameter value the map has two coexisting one-band chaotic attractors. Indeed, as one can see in Figs. 4(b) and (c), the intervals $[c_{\mathcal{R}}^1, c_{\mathcal{R}}^2]$ and $[c_{\mathcal{L}}^2, c_{\mathcal{L}}^1]$ are invariant and absorbing. As the function $f^{m/2}$ is everywhere expanding in these intervals, the intervals represent chaotic attractors. Moreover, it follows immediately from the shape of the function $f^{m/2}$ in these intervals, that the density distributions on these attractors are highly non-equal. In particular, in the middle part of the chaotic attractor $[c_{\mathcal{R}}^1, c_{\mathcal{R}}^2]$ there is a subinterval $[c_{\mathcal{R}}^4, c_{\mathcal{R}}^3]$ confined by the minimal and maximal values of the corresponding branches as indicated in Fig. 4(b). As one can see in this figure, the points of this interval have a significantly smaller number of preimages inside the absorbing interval $[c_{\mathcal{R}}^1, c_{\mathcal{R}}^2]$ than the points of the complementary set $[c_{\mathcal{R}}^1, c_{\mathcal{R}}^2] \setminus [c_{\mathcal{R}}^4, c_{\mathcal{R}}^3]$. Accordingly, the density in the interval $[c_{\mathcal{R}}^4, c_{\mathcal{R}}^3]$ is much lower than in other parts of this attractor. A similar reasoning applies to the other chaotic attractor $[c_{\mathcal{L}}^2, c_{\mathcal{L}}^1]$ (see Fig. 4(c)).

Note also that in addition to two chaotic attractors, the interval $[c_{\mathcal{R}}^1, c_{\mathcal{L}}^1]$ contains also a chaotic repeller. Indeed, let x^* be the fixed point belonging to the branch of $f^{m/2}$ which is most close from the right side to the interval $[c_{\mathcal{R}}^1, c_{\mathcal{R}}^2]$ and has the range $[c_{\mathcal{R}}^1, c_{\mathcal{L}}^1]$ (see Fig. 4(a)). Similarly, let x^{**} be the fixed point belonging to the branch of $f^{m/2}$ which is most close from the left side to the interval $[c_{\mathcal{L}}^2, c_{\mathcal{L}}^1]$ and has the range $[c_{\mathcal{R}}^1, c_{\mathcal{L}}^1]$. It can easily be shown that these fixed points, as well as all other fixed points which belong to the branches with the range $[c_{\mathcal{R}}^1, c_{\mathcal{L}}^1]$ are homoclinic. Therefore, the interval $[x^*, x^{**}]$ does necessarily contain a set on which the map $f^{m/2}$ is chaotic [30]. As the interval $[x^*, x^{**}]$ is not absorbing (since it contains values x' with $f(x') \notin [x^*, x^{**}]$), this set is a chaotic repeller. Accordingly, some of the transformations of chaotic attractors discussed below are caused by interactions of the chaotic attractors with this chaotic repeller.

It is clearly visible in Fig 3(d) that as Γ is increased to the point marked with B_1 in this figure, the lower chaotic attractor shrinks in size. The reason for that can be seen in Fig. 4(d) which shows the function $f^{m/2}$ at the corresponding parameter value. Indeed, the overall shape of the function $f^{m/2}$ does not significantly change compared with the one shown in Fig. 4(a), but the number of spikes in the interval $[c_{\mathcal{R}}^1, c_{\mathcal{R}}^2]$ decreases, and in particular, there are no spikes in the interval $[c_{\mathcal{R}}^3, c_{\mathcal{R}}^2]$ (see Fig. 4(e)). As a consequence, the typical initial values from the interval $[c_{\mathcal{R}}^1, c_{\mathcal{R}}^3)$ are mapped in the interval $[c_{\mathcal{R}}^3, c_{\mathcal{R}}^2]$, which is now invariant and forms a chaotic attractor. Note also that the interval $[c_{\mathcal{R}}^1, c_{\mathcal{R}}^3)$ contains still a spike which intersects the diagonal. Accordingly, there are still repelling fixed points in this interval. Moreover, it can be easily shown that these fixed points are homoclinic, so it follows from the results proven in [30] that a chaotic repeller exists in a neighborhood of the homoclinic orbits to these fixed points. Clearly, the points of this repeller and their preimages in the interval $[c^1_{\mathcal{R}}, c^3_{\mathcal{R}})$ are the atypical initial values from the interval $[c^1_{\mathcal{R}}, c^3_{\mathcal{R}})$ which are not mapped in chaotic attractor given by the interval $[c^3_{\mathcal{R}}, c^2_{\mathcal{R}}]$.

For further increasing values of Γ, the spikes appear in the interval $[c^3_{\mathcal{R}}, c^2_{\mathcal{R}}]$, so that eventually the lower chaotic attractor restores its size and becomes $[c^1_{\mathcal{R}}, c^2_{\mathcal{R}}]$ again. Moreover, as one can see in Fig. 4(f), spikes appear also on the upper attractor. As a consequence, this attractor is no longer given by the interval $[c^2_{\mathcal{L}}, c^1_{\mathcal{L}}]$ but instead by $[c^5_{\mathcal{L}}, c^1_{\mathcal{L}}]$, where $c^5_{\mathcal{L}}$ is the minimal value of the spikes in the interval $[c^2_{\mathcal{L}}, c^1_{\mathcal{L}}]$. This explains also why the density of this chaotic attractor has a highly unequal distribution. Indeed, as one can see in Fig. 4(g), there are only two spikes in the interval $[c^2_{\mathcal{L}}, c^1_{\mathcal{L}}]$, with very small domains, and the only way for an orbit to reach the interval $[c^5_{\mathcal{L}}, c^2_{\mathcal{L}})$ is to be mapped previously to a suitable part of these (already very small) domains. Accordingly, the invariant density of the attractor in the interval $[c^5_{\mathcal{L}}, c^2_{\mathcal{L}})$ is much lower than in the interval $[c^2_{\mathcal{L}}, c^1_{\mathcal{L}}]$.

As Γ increases further, two coexisting chaotic attractors $[c^1_{\mathcal{R}}, c^2_{\mathcal{R}}]$ and $[c^5_{\mathcal{L}}, c^1_{\mathcal{L}}]$ persist but the spikes belonging to the upper attractors grow. Then, as illustrated in Fig. 4(h), the lower boundary of the attractor (the critical value $c^5_{\mathcal{L}}$) reaches the repelling fixed point x^{**}. The condition

$$c^5_{\mathcal{L}} = x^{**} \tag{4}$$

corresponds to a homoclinic bifurcation of this fixed point, which (being one-side homoclinic before this bifurcation) becomes two-side homoclinic after. Accordingly, as illustrated in Fig. 4(i), the interval $[c^5_{\mathcal{L}}, c^1_{\mathcal{L}}]$ is no longer invariant after the bifurcation, so that the described homoclinic bifurcation of x^{**} causes a final bifurcation of the chaotic attractor. After this bifurcation occurs, the chaotic attractor does not exist any longer, and the interval $[x^{**}, c^1_{\mathcal{L}}]$ contains points of a chaotic repeller (more precisely, the chaotic repeller which was confined before the bifurcation in the interval $[x^*, x^{**}]$, expands after the bifurcation to the interval $[x^*, c^1_{\mathcal{L}}]$). Hence, a typical initial value from the interval $[c^5_{\mathcal{L}}, x^{**})$ converges eventually to the chaotic attractor $[c^1_{\mathcal{R}}, c^2_{\mathcal{R}}]$, which is now the only attractor. However, an orbit started at an initial value in the interval $(x^{**}, c^1_{\mathcal{L}}]$ may remain in this interval for a quite long time, showing the so-called *transient chaos* [31,32]. Indeed, it is clearly visible in Fig. 4(i) that there are three spikes in the interval $(x^{**}, c^1_{\mathcal{L}}]$, and that the only way for an orbit to leave this interval is to reach a points x' with $f^{m/2}(x') < x^{**}$ which necessarily belongs to the domain of one of the spikes.

With increasing Γ the chaotic attractor $[c^1_{\mathcal{R}}, c^2_{\mathcal{R}}]$ remains the only attractor in a quite large parameter interval, as illustrated in Fig. 5(a)–(c). In fact, in this parameter interval the function $f^{m/2}$ undergoes some significant transformations, which, however, influence the structure of the chaotic repeller only. It can be clearly seen in Fig. 5(a) that the spikes in the interval $[x^{**}, c^1_{\mathcal{L}}]$ which have previously caused the final bifurcation described above continue to increase in size and in number. At the parameter value corresponding to Fig. 5(b) the ranges of the corresponding branches cover already the complete interval $[c^1_{\mathcal{R}}, c^1_{\mathcal{L}}]$, while at the parameter value corresponding to Fig. 5(c) these branches do not intersect the diagonal any longer. Clearly, the disappearance of the fixed points belonging to these branches is associated with homoclinic bifurcations which change the structure of the chaotic repeller but do not affect the chaotic attractor. Finally, the function $f^{m/2}$ takes the configuration shown in Fig. 5(d), with the major part of branches having the same range as the branches in the interval $[c^1_{\mathcal{R}}, c^2_{\mathcal{R}}]$, and a couple of spikes whose range decreases with increasing Γ.

As already mentioned, the described transformations of the shape of the function $f^{m/2}$ do not influence the chaotic attractor, which remains to be given by the interval $[c^1_{\mathcal{R}}, c^2_{\mathcal{R}}]$. This changes at the parameter value at which the spikes begin to grow in this interval (see Fig. 5(d)). As one can see in the magnification shown in Fig. 5(e), thereafter the upper boundary of the chaotic attractor is given by the critical values $c^5_{\mathcal{R}}$. As at the beginning there are only a few spikes, the density of the attractor is almost completely concentrated in the part of the attractor given by the former ranges $[c^1_{\mathcal{R}}, c^2_{\mathcal{R}}]$, while the density in the interval $(c^2_{\mathcal{R}}, c^5_{\mathcal{R}}]$ is very low. Then, the condition

$$c^5_{\mathcal{R}} = x^*$$

signifies a homoclinic bifurcation of the fixed point x^* which becomes two-side homoclinic (in other words, at this point a chaotic attractor merges with a chaotic repeller), as illustrated in Fig 3(e) and Figs. 5(c),(d). Accordingly, as the fixed point has a positive eigenvalue, the chaotic attractor expands suddenly to the full range $[c^1_{\mathcal{R}}, c^1_{\mathcal{L}}]$, i.e., undergoes an expansion bifurcation ([28,27]) and after that, the interval $[c^1_{\mathcal{R}}, c^5_{\mathcal{R}}]$ is no longer invariant (see Fig. 5(e),(f)).

For larger values of Γ (in the parameter range indicated by the rectangle R_4 in Fig. 3(c) and shown magnified in Fig. 3(f)), one can observe also a merging bifurcation ([28,27]) associated with a homoclinic bifurcation of the fixed point x^{**}. Note that the shape of the bifurcation diagram close to this bifurcation differs quite significantly from the typical shapes related to merging bifurcations. However, it is easy to see that the fixed point x^{**} has a negative eigenvalue, as required for merging bifurcations, and the unusual shape of the bifurcation diagram is in fact explained by the high absolute value of the slope of the branch containing this fixed point. As soon as the preimage of the critical value defining the boundary of the low-density part of the chaotic attractor reaches the domain of this branch, a slightest parameter variation causes a significant movement of this boundary, reflected in an almost vertical edge in the bifurcation diagram (see also [24]).

To summarize, all three standard types of transformations of chaotic attractors in 1D maps (the merging, the expansion and the final bifurcations) occur in the considered system, and qualitatively they occur as described in the literature [28]. However, quantitatively the situation is quite different from the known examples, since the parts of the chaotic attractors involved in these bifurcations have an extremely low density. The reasons for that are related with the spiking phenomenon. Still, the question remains open, which reasons cause the spikes to appear?

4 Appearance of the spikes

A wide-spread approach for a qualitative study of the dynamics of 1D maps are so-called cobweb diagrams, which show the behavior of orbits in a compact form on the graph of the function. However, for the function $f^{m/2}$ this approach is practically not applicable due to a very high number of its branches and their extremely small domains. To solve this problem, we suggest a slightly modified technique which can be seen as a natural extension of the usual cobweb diagrams.

Recall that the function F is non-autonomous and depends on two arguments, x and k. However, as the argument k takes integer values between 0 and $\frac{m}{2}-1$, the function F can also be seen as a set of $\frac{m}{2}$ functions F_k, $k=0,\ldots,\frac{m}{2}-1$, each of which depends on one argument x only. For each fixed k, the function $F_k(x)$ is bimodal, with a local maximum at the border point b_k^- and a local minimum at b_k^+. Accordingly, the overall function F has m border points b_k^-, b_k^+, as illustrated in Fig. 7 (see also Fig. 2). As one can see in Fig. 7(a) and the magnifications shown in Fig. 7(b),(c), with k increasing from zero to $m/4$ (a half of the period of the function F with respect to k), the function F_k is translated upwards and to the right, and thereafter (in the second half-period) it is translated downwards and to the left. Accordingly, in Fig. 7(a)–(c), the top-most function is F_{50} and the low-most is F_0.

In the presented setup, the cobweb diagrams can be presented as follows. Recall, that in the usual cobweb diagrams an orbit moves from a point on the diagonal vertically to the value of the function at this point, then horizontally to the diagonal, to the function again, and so on. For map F, the diagram is produced similarly, with the difference that an orbit moves from a point on the diagonal to the value of the function F_k, then to the diagonal and to the value of the *next* function $F_{k+1 \bmod m/2}$, and so on. As an example, Fig. 7(d) illustrates an unstable $m/2$-cycle of map (2) presented in this way.

Now let us turn back to the mechanism leading to the appearance of spikes in the function $f^{m/2}$. Recall that the function $f^{m/2}$ is an iterate of the function F. Therefore, the border points of $f^{m/2}$ are *preimages* of the border points of F, and the values of $f^{m/2}$ at these border points are *images* of the border points of F [27]. Clearly, by monotonicity of all branches of $f^{m/2}$, the tips of the spikes are located at the border points of $f^{m/2}$. Using the described extension of the cobweb diagrams, we can determine to which border points of F the spikes are related.

As an example, let us consider now the shape of the function $f^{m/2}$ in the same interval at two parameter values, before and after the appearance of spikes, as shown in Fig. 6(a) and (b), respectively. In fact, the parameter value chosen in Fig. 6 is the same as in Fig. 4(g), so the four spikes shown there are related to the final bifurcation discussed above. The border points of $f^{m/2}$ corresponding to the tips of these spikes are

$$\begin{aligned} x_0^{(1)} &\approx 0.0235366, & x_0^{(2)} &\approx 0.0237158, \\ x_0^{(3)} &\approx 0.0238224, & x_0^{(4)} &\approx 0.0240122. \end{aligned} \tag{5}$$

Using the extended cobweb diagrams, it can be easily shown that in a few iterations these border points are mapped on the same border point of map F. Indeed, as shown in Fig. 8(a), in one step they are mapped pairwise together:

$$
\begin{aligned}
F^{\mathcal{M}}_{50}(x_0^{(1)}) =& F^{\mathcal{R}}_{50}(x_0^{(4)}) := x_1^{(1/4)},\\
F^{\mathcal{M}}_{50}(x_0^{(2)}) =& F^{\mathcal{R}}_{50}(x_0^{(3)}) := x_1^{(2/3)}.
\end{aligned}
$$

Thereafter, the points $x_1^{(1/4)}$ and $x_1^{(2/3)}$ are mapped by the function $F^{\mathcal{M}}_{51}(x)$, so that

$$x_2^{(1/4)} := F^{\mathcal{M}}_{51}(x_1^{(1/4)}), \quad x_2^{(2/3)} := F^{\mathcal{M}}_{51}(x_1^{(2/3)}).$$

Eventually, as illustrated in Fig. 8(b), after one more step performed by the function $F^{\mathcal{M}}_{52}$ the orbits started at all four points $x_0^{(j)}$, $j = 1, 2, 3, 4$, coincide:

$$F^{\mathcal{M}}_{52}(x_2^{(1/4)}) = F^{\mathcal{R}}_{52}(x_2^{(2/3)}) := x_3^{(1/2/3/4)}.$$

Moreover, as illustrated in Fig. 8(b) as well, after one more iteration the point $x_3^{(1/2/3/4)}$ is mapped on the border point b^+_{54} of the function $F_{54}(x)$:

$$F^{\mathcal{M}}_{53}(x_3^{(1/2/3/4)}) = b^+_{54},$$

that means for all four points $x_0^{(j)}$, $j = 1, 2, 3, 4$, that

$$F_{53} \circ F_{52} \circ F_{51} \circ F_{50}(x_0^{(j)}) = b^+_{54}.$$

Therefore, the border points of $f^{m/2}$ specified in Eq. (5) are in fact given by the preimages of the border point b^+_{54} as follows:

$$
\begin{aligned}
x_0^{(1)} &= (F^{\mathcal{M}}_{50})^{-1} \circ (F^{\mathcal{M}}_{51})^{-1} \circ (F^{\mathcal{M}}_{52})^{-1} \circ (F^{\mathcal{M}}_{53})^{-1}(b^+_{54}),\\
x_0^{(2)} &= (F^{\mathcal{M}}_{50})^{-1} \circ (F^{\mathcal{M}}_{51})^{-1} \circ (F^{\mathcal{R}}_{52})^{-1} \circ (F^{\mathcal{M}}_{53})^{-1}(b^+_{54}),\\
x_0^{(3)} &= (F^{\mathcal{R}}_{50})^{-1} \circ (F^{\mathcal{M}}_{51})^{-1} \circ (F^{\mathcal{R}}_{52})^{-1} \circ (F^{\mathcal{M}}_{53})^{-1}(b^+_{54}),\\
x_0^{(4)} &= (F^{\mathcal{R}}_{50})^{-1} \circ (F^{\mathcal{M}}_{51})^{-1} \circ (F^{\mathcal{M}}_{52})^{-1} \circ (F^{\mathcal{M}}_{53})^{-1}(b^+_{54}).
\end{aligned}
\tag{6}
$$

Next, to explain the appearance of spikes, we have to trace the value $c^5_{\mathcal{L}}$ of the iterate at these border points, i.e., the value

$$c^5_{\mathcal{L}} = f^{m/2}(x_0^{(j)}), \quad j = 1, 2, 3, 4.$$

Note that here we assume implicitly that this value is the same for all four considered points. As shown below, this is indeed the case. Recall also that the value $c^5_{\mathcal{L}}$ is involved in the final bifurcation discussed in the previous section (see condition (4)). By definition of the iterate this value is given by

$$
\begin{aligned}
c^5_{\mathcal{L}} =& F_{49} \circ F_{48} \circ \cdots \circ F_1 \circ F_0 \circ F_{99} \circ F_{98} \circ \cdots \circ\\
& F_{54} \circ F_{53} \circ F_{52} \circ F_{51} \circ F_{50}(x_0^{(j)}).
\end{aligned}
\tag{7}
$$

However, as all four points $x_0^{(j)}$, $j = 1, 2, 3, 4$, are mapped within the first three iterations on the same border point b^+_{54}, it follows from Eqs. (6) and (7) that

$$c^5_{\mathcal{L}} = F_{49} \circ F_{48} \circ \cdots \circ F_{55} \circ F_{54}(b^+_{54}).$$

Noteworthy, this proves that the values at the tips of all four spikes are identical as well.

In a similar way, the values at the other border points of $f^{m/2}$ can be determined, in particular at the border points located close to the spikes described above. Using the extended cobweb diagrams starting at these border points one can show that these points are preimages of the border points of F different from b^+_{54}. For example, the critical values $c^1_{\mathcal{L}}$, $c^2_{\mathcal{L}}$ (see Fig. 6) turn out to be given by:

$$
\begin{aligned}
c^1_{\mathcal{L}} &= F_{49} \circ F_{48}(b^+_{48}),\\
c^2_{\mathcal{L}} &= F_{49} \circ F_{48} \circ F_{47} \circ F_{46}(b^+_{46}).
\end{aligned}
$$

A direct computation shows that at the parameter value corresponding to Fig. 6(a), the value $c^5_{\mathcal{L}}$ satisfies

$$c^2_{\mathcal{L}} < c^5_{\mathcal{L}} < c^1_{\mathcal{L}}.$$

However, with increasing $\mathit{\Gamma}$, the value $c^5_{\mathcal{L}}$ decreases are eventually reaches $c^2_{\mathcal{L}}$. Accordingly, the appearance of spikes is associated with the condition

$$c^2_{\mathcal{L}} = c^5_{\mathcal{L}},$$

so that they exist for $c^5_{\mathcal{L}} < c^2_{\mathcal{L}}$ and do not exist otherwise. In other words, the appearance of spikes is explained by the fact that the location of the images of specific border points of F with respect to each other changes under parameter variation.

In more general terms, the mechanism leading to the appearance of spikes can be summarized as follows. Let $\mathcal{A}$ be a chaotic attractor of map $f^{m/2}$ and $\mathcal{B} = \{b^0, b^1, \ldots, b^n\}$ be the set of border points of $f^{m/2}$ inside $\mathcal{A}$. Clearly, the lower and the upper boundaries of $\mathcal{A}$ are giver by

$$c^{\min} = \min_j f^{m/2}(b^j), \quad c^{\max} = \max_j f^{m/2}(b^j).$$

Suppose, for almost all j the border points $b^j \in \mathcal{B}$ are given by preimages of a few border points of F. However, there are also a few border points $b^\ell \in \mathcal{B}$ defined by preimages of a different border point of F. As long as the value $f^{m/2}(b^\ell)$ belongs to the interval $[c^{\min}, c^{\max}]$, there are no spikes. As soon as the value $f^{m/2}(b^\ell)$ exceeds this interval, spikes appear.

5 Preconditions for spiking

So far we have shown that the appearance of the spiking phenomenon can be explained by the fact that specific images of some border points of F change their locations with respect to each other. In practical situations, this result, although mathematically correct, is not particularly useful, since one does not know *a priori* which images of which border points are to be considered. Moreover, the question is still open in which class of maps this effect occurs. First, it can be shown that the appearance of spikes is not related to the non-linearity of the function $F^{\mathcal{M}}$ in Eq. (2). Indeed, if this function is replaced by its linear approximation, no significant changes regarding the low-density parts of chaotic attractors can be observed. Therefore, it is justified to consider a piecewise linear model which differs from map F quite significantly but still exhibits the spiking phenomenon.

Among 1D piecewise linear maps, the most known is the standard tent map defined by

$$x_{k+1} = \Lambda(x_k) = \alpha\left(\tfrac{1}{2} - \left|x_k - \tfrac{1}{2}\right|\right). \tag{8}$$

The shape of the m-th iterate Λ^m, for $a = 1.14$ and $m = 100$, is shown in Fig. 9. As one can see, this function has a shape quite similar to the one of the function $f^{m/2}$ considered in the previous sections. Indeed, in the presented example, the major part of the branches have the ranges confined to four intervals corresponding to the bands of the 4-band chaotic attractor of map (8) existing at the considered parameter value. Only a few branches have larger ranges, and it is easy to see that they contain the repelling fixed point and the repelling 2-cycle of map (8), as well as their preimages. However, it is well known that chaotic attractors of the tent map do not contain any low-density parts. Accordingly, no one of the large-range branches are located in the intervals corresponding to the bands of the chaotic attractor, and no spikes exist.

Among the differences between the map (2) and the tent map (8), the one which appears to be responsible for the existence of spikes in map (2) and their absence in map (8), is that map (8) is autonomous while map (2) is not. To confirm that let us introduce the following non-autonomous extension of the tent map:

$$\begin{aligned} x_{k+1} &= h(x_k) \\ &= \left(\alpha + \beta\sin\left(\frac{2\pi k}{m}\right)\right)\left(\tfrac{1}{2} - \left|x_k - \tfrac{1}{2}\right|\right), \end{aligned} \tag{9}$$

with $\beta \ll \alpha$. As one can see comparing Eqs. (8) and (9), instead of a constant parameter α in map (8), the corresponding term in map (9) oscillates around the value α with a small amplitude β and the period m.

Recall that for map (8), the maximal value of the function is given by $\Lambda(\frac{1}{2}) = \frac{1}{2}\alpha$. For map (9), this value oscillates in the interval

$$\left[\tfrac{1}{2}(\alpha - \beta), \tfrac{1}{2}(\alpha + \beta)\right].$$

Consequently, the absorbing interval $[h^2(\frac{1}{2}), h(\frac{1}{2})]$ in which the dynamics of map (9) is confined, has oscillating boundaries, similar to map (2). In several other respects, maps (9) and (2) differ quite significantly: for each fixed k map (9) is unimodal while map (2) is bimodal; under variation of k the absorbing interval of map (9) grows and shrinks in size, while for map (2) it moves to the left and to the right preserving its size, and so on.

Clearly, for $\beta = 0$, map (9) is identical with map (8) and shows neither the spiking phenomenon nor the low-density parts of chaotic attractor. As an illustration, Fig. 10(a) shows a part of the bifurcation diagram of the tent map containing two-band chaotic attractors. Although the invariant density of the bands has a non-uniform distribution, the differences in the density inside the bands are not significant. By contrast, map (9) with $\beta > 0$ shows in the same parameter range two-band chaotic attractors with extreme differences in the density inside the bands, as illustrated by the bifurcation diagram in Fig. 10(b). In fact, the presented bifurcation diagram has been calculated using 100 000 000 iteration steps of map (9), and this high number of iteration is indeed necessary, as the results obtained using a smaller number of iterations can easily be mistaken for four-band chaotic attractors. The reasons for that can easily be understood comparing the shapes of the functions Λ^m and h^m. Indeed, the overall shape of these functions is almost the same (see Figs. 10(c) and (d)). However, as illustrated in Figs. 10(e) and (f), using a sufficient magnification one can see that the shapes on the microscopic level differ significantly. For map (8), each of the bands of the chaotic attractor is covered by the majority of the branches of Λ^m. For map (9), the situation is essentially different. The majority of the branches have the ranges covering only the upper or only the lower parts of the attractor, while the middle part of the band is reachable via a small number of branches only. As one can see, some of these branches belong to spikes, while the other connect the lower and the upper parts of the attractor. In any case, there are only a few of such branches, the union of their domains covers a small fraction of the attractor, and therefore, the density in the middle part of the bands is much lower (at some parameter values by factor 10^3) than in the upper and the lower parts.

The presented example can be seen as a confirmation that the appearance of spiking phenomenon is related to the presence of low frequency oscillations. Indeed, as soon as the low frequency oscillations of the absorbing interval are introduced, even such a simple model as the tent map starts to show the spiking phenomenon and the resulting low density parts of chaotic attractor. This is also consistent with the fact that the presence of the low frequency causes the function to have a number of critical points which were not present before, and a complex interplay between their images becomes possible, leading in some configuration to the appearance of spikes.

6 Summary

A boost PFC AC-DC power converter can substantially improve the power factor and reduce the harmonic distortion. Converters of this type use a switching element to force the input AC current to be sinusoidal and in phase with the input voltage and play an important role in modern power electronics applications. The initial motivation behind this work was to reconsider the transformations of chaotic attractor in a model of a PFC AC-DC converter which have already been reported in [25] but not completely understood. To explain the mechanisms leading to these transformations we applied the recently developed two-step modeling approach [21–23] consisting of the calculation of a primary stroboscopic mapping with the sampling rate determined by the high switching frequency followed by the calculation of the secondary stroboscopic mapping with the sampling rate determined by the low switching frequency. Note that this modeling approach has been developed for DC-AC converters, and in this work we demonstrated for the first time that it can be applied to AC-DC converters as well. As the behavior of converters of both classes is essentially determined by two vastly different frequencies, it is not surprising that ultimately their discrete-time models belong to the same class of maps, characterized by the presence of an extremely high number of switching manifolds.

Using the obtained model, we have shown that to explain the observed transformations of chaotic attractors it is necessary to take into account the parts of these attractors characterized by an ultra-low invariant density. Indeed, as reported in [24], the homoclinic bifurcations leading to the transformations of chaotic attractors may occur in such parts of the attractors and their effect becomes visible for parameter values quite far away from the bifurcation point. Similar to the models of DC-AC converters discussed in the cited work, the model considered in the present paper exhibits all three types of transformations of chaotic attractors (the expansion, the merging and the final bifurcations) typical for 1D maps and these bifurcations are associated with extreme differences in the attractors' invariant density. It has been already shown in [24] that this effect is caused by the spiking phenomenon. In the present work we have pointed out that this phenomenon causes also the transient chaos to occur.

To explain the mechanism leading to the spiking effect, we developed an extension of the usual cobweb diagrams, making them applicable to non-autonomous maps with a periodic dependency on the discrete time variable k. Applying this extension we traced the way to the values defining the tips of the spikes from the border points of the primary stroboscopic mapping which determine these values. It turned out that in the configuration of the parameters related to the appearance of spikes, among a multitude of border points of the secondary stroboscopic mapping a few are determined by the images of a single border point of the primary stroboscopic, while the other are determined by some others. In this way we have demonstrated how, under parameter variation, a displacement of specific images of the critical points of the map leads to the spiking effect. We have also provided at least a clear evidence that this effect is a consequence of the presence of two vastly different frequencies governing the dynamics, and is therefore quite generic for the considered class of models.

7 Acknowledgments

The authors are grateful to Mike Jeffrey from the University of Bristol and Soumitro Banerjee from the Indian Institute of Science Education & Research – Kolkata for fruitful discussions.

The work of V. Avrutin was supported by the German Research Foundation within the scope of the project "Generic bifurcation structures in piecewise-smooth maps with extremely high number of

borders in theory and applications for power converter systems".

References

1. B. K. Bose. Power electronics and motor drives recent progress and perspective. *IEEE Transactions on Industrial Electronics*, 56(2):581–588, 2009.
2. B. K. Bose. Power electronics in smart grid and renewable energy systems. *Proceedings of the IEEE*, 105(11):2007–2010, 2017.
3. M. Truntič, T. Konjedic, M. Milanovič, P. Šlibar, and M. Rodič. Control of integrated single-phase PFC charger for EVs. *IET Power Electronics*, 11(11):1804–1812, 2018.
4. M. Bodetto, A. El Aroudi, A. Cid-Pastor, and M. S. Al-Numay. Improving the dimming performance of low-power single-stage AC-DC HBLED drivers. *IEEE Transactions on Industrial Electronics*, 64(7):5797–5806, 2017.
5. S. Banerjee and G. C. Verghese. *Nonlinear Phenomena in Power Electronics – Attractors, Bifurcations, Chaos, and Nonlinear Control.* IEEE Press, 2001.
6. Zh.T. Zhusubaliyev and E. Mosekilde. *Bifurcations and Chaos in piecewise-smooth dynamical systems*, volume 44 of *Nonlinear Science A*. World Scientific, 2003.
7. P.C. Todd. UC3854 controlled power factor correction circuit design. *UNITRODE application note U-134*, pages 10–303, 1999.
8. O. García, J. A. Cobos, R. Prieto, P. Alou, and J. Uceda. Single phase power factor correction: A survey. *IEEE Trans. on Power Electronics*, 18(3):749–755, 2003.
9. M. Orabi and T. Ninomiya. Non-linear dynamics of power factor correction converter. *IEEE Trans. on Industrial Electronics*, 50(6):1116–1125, 2003.
10. H. H. C. Iu, Y. Zhou, and C. K. Tse. Fast-scale instability in a boost PFC converter under average current control. *Int. J. Circ. Theor. Appl.*, 31:611–624, 2003.
11. M. Orabi and T. Ninomiya. Stability investigation of the cascade two-stage PFC converter. *IEICE Transactions on Communications*, E8-B(12):3506–3514, 2004.
12. X. Wu X., C. K. Tse, S. C. Wong, and J. Lu. Fast-scale bifurcation in single-stage PFC power supplies operating with dcm boost stage and CCM forward stage. *Int. J. of Circ. Theor. Appl.*, 2006.
13. S. C. Wong, C. K. Tse, M. Orabi, and T. Ninomiya. The method of double averaging: An approach for modeling power-factor-correction switching converters. *IEEE Trans. on Circuits and Systems*, 53(2):454–462, 2006.
14. A. El Aroudi, M. Orabi, and L. Martínez-Salamero. A representative discrete-time model for uncovering slow and fast scale instabilities in boost power factor correction AC-DC pre-regulators. *Int. J. Bifurcation Chaos*, 18(10):3073–3092, 2008.
15. G. Chu, C. K. Tse, and S.-C Wong. Line-frequency instability of PFC power supplies. *IEEE Trans. on Power Electronics*, 24(2):469–482, 2009.
16. E. Fossas and G. Olivar. Study of chaos in the buck converter. *IEEE Trans. Circ. & Sys. I*, 43:13–25, 1996.
17. S. Banerjee, P. Ranjan, and C. Grebogi. Bifurcations in Two-Dimensional Piecewise Smooth Maps - Theory and Applications in Switching Circuits. *IEEE Trans. Circ. & Sys. I*, 47:633–643, 2000.
18. A. El Aroudi, L. Benadero, E. Toribio, and G. Olivar. Hopf bifurcation and chaos from torus breakdown in a PWM voltage-controlled dc-dc boost converter. *IEEE Trans. Circ. & Sys. I*, 1999.
19. Zh.T. Zhusubaliyev, E. A. Soukhoterin, and E. Mosekilde. Border-collision bifurcations and chaotic oscillations in a piecewise-smooth dynamical system. *Int. J. Bifurcation Chaos*, 11:2977–3001, 2001.
20. A. El Aroudi, M. Debbat, G. Olivar, L. Benadero, and R. Giralt E. Toribio. Bifurcations in DC-DC switching converters: Review of methods and applications. *Int. J. Bifurcation Chaos*, 15:1549–1578, 2005.
21. V. Avrutin, E. Mosekilde, Zh.T. Zhusubaliyev, and L. Gardini. Onset of chaos in a single-phase power electronic inverter. *Chaos*, 25:043114, 2015.
22. V. Avrutin, Zh.T. Zhusubaliyev, and E. Mosekilde. Border collisions inside the stability domain of a fixed point. *Physica D*, 321-322:1–15, 2016.
23. V. Avrutin, Zh.T. Zhusubaliyev, and E. Mosekilde. Cascades of alternating pitchfork and flip bifurcations in H-bridge inverters. *Physica D*, 345:27–39, 2017.
24. V. Avrutin, Zh.T. Zhusubaliyev, D. Suissa, and A. El Aroudi. Non-observable chaos in piecewise smooth systems. *Nonlinear Dynamics*, 2019.
25. V. Avrutin, Zh.T. Zhusubaliyev, A. El Aroudi, D. Fournier-Prunaret, G. Garcia, and E. Mosekilde. Disrupted bandcount doubling in an AC-DC boost PFC circuit modeled by a time varying map. *J. of Physics*, 692(1):012003, 2016.
26. I. Sushko, V. Avrutin, and L. Gardini. Bifurcation structure in the skew tent map and its application as a border collision normal form. *J. of Diff. Equations and Applications*, 22(8):1040–1087, 2016.
27. V. Avrutin, L. Gardini, I. Sushko, and F. Tramontana. *Continuous and Discontinuous Piecewise-Smooth One-dimensional Maps: Invariant Sets and Bifurcation Structures.* Nonlinear Science, Series A. World Scientific, 2019.
28. V. Avrutin, L. Gardini, M. Schanz, and I. Sushko. Bifurcations of chaotic attractors in one-dimensional maps. *Int. J. Bif. Chaos*, 24(8):1440012, 2014.
29. N. Metropolis, M. L. Stein, and P. R. Stein. On Finite Limit Sets for Transformations on the Unit Interval. *J. Comb. Theory*, A15:25–44, 1973.
30. L. Gardini, I. Sushko, V. Avrutin, and M. Schanz. Critical homoclinic orbits lead to snap-back repellers. *Chaos, Solitons & Fractals*, 44:433–449, 2011.
31. C. Grebogi, E. Ott, and J. A. Yorke. Crisis: sudden changes in chaotic attractors and transient chaos. *Physica D*, 7:181, 1983.
32. Y.Ch. Lai and T. Tél. *Transient chaos: complex dynamics on finite time scales*, volume 173. Springer Science & Business Media, 2011.

List of Figures

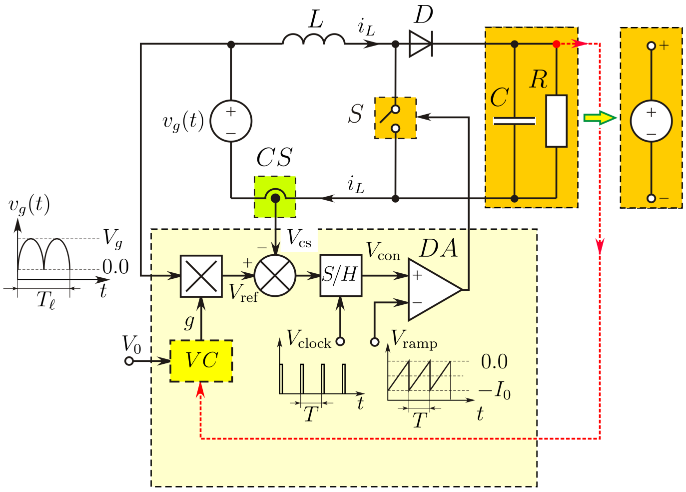

Fig. 1 Schematic diagram of the considered AC-DC converter. CS is the current sensor, S/H is the sample-and-hold unit, and VC is the voltage controller. $v_g(t) = V_g|\sin(\omega_l t)|$ is the rectified sinusoidal source voltage, where V_g is a constant amplitude and $\omega_l = \frac{2\pi}{T_\ell}$. V_0 is the output voltage supposed to be constant for simplicity.

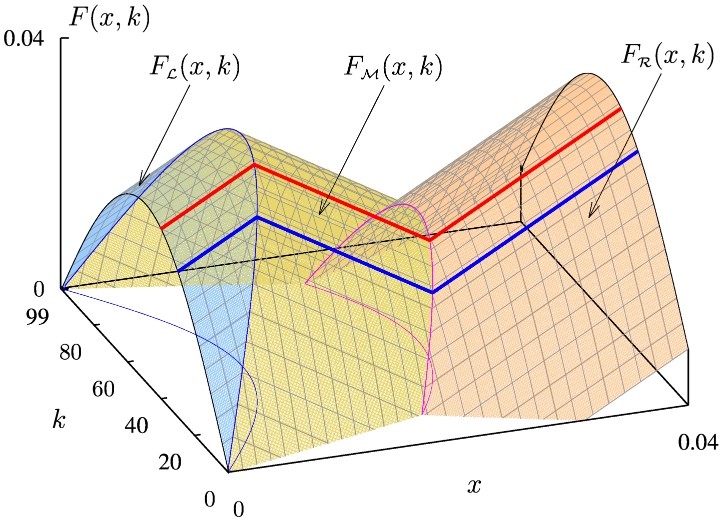

Fig. 2 Function $F_k(x)$ given by Eq. (2) depending on x and k for $0 \leqslant k < \frac{1}{2}m$. Additionally, the bimodal functions $F(x, 30)$ and $F(x, 40)$ are indicated.

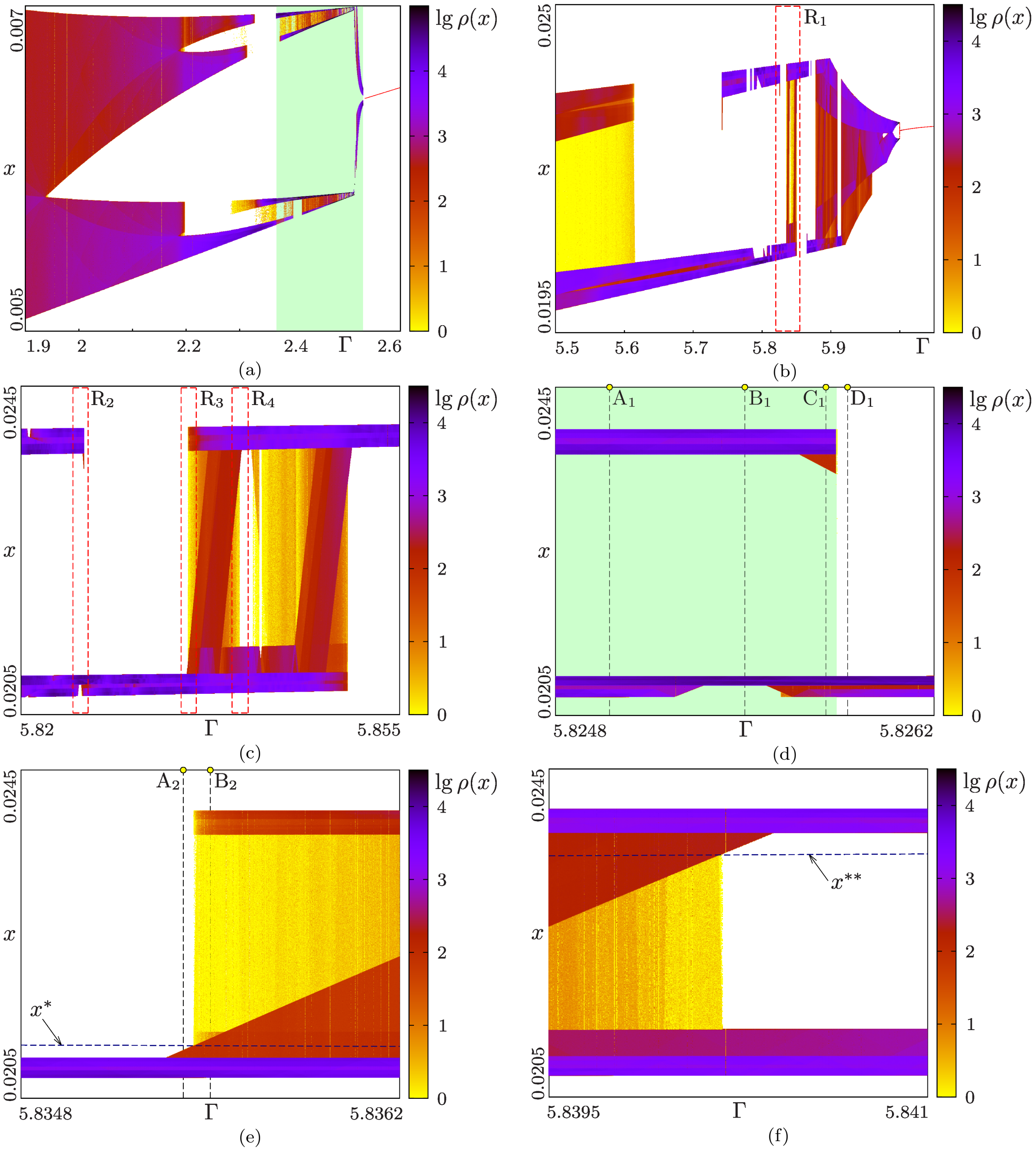

Fig. 3 Bifurcation diagrams for map (2) calculated using the secondary stroboscopic map (3) at (a) $m = 1000$ and (b) $m = 200$. The rectangle R_1 outlined in (b) is shown magnified in (c), the rectangles $\mathrm{R}_{2,3,4}$ outlined in (c) and are magnified in (d), (e) and (f), respectively. The invariant density of the attractors corresponds to color bars. In (a) and (d), the bistability intervals are indicated by the background color.

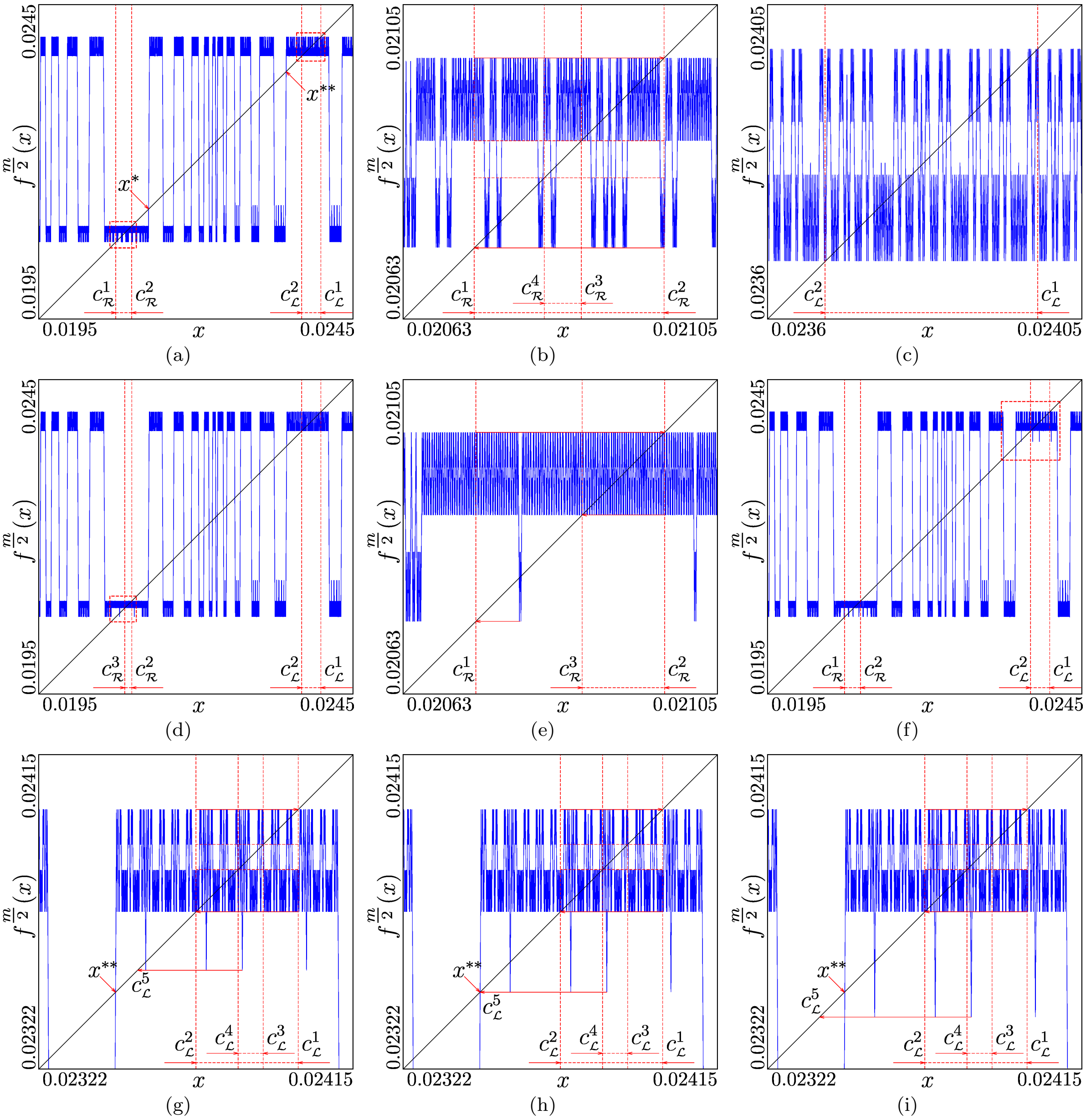

Fig. 4 (a) Function $f^{m/2}$ at the parameter value $\mathit{\Gamma} = 5.825$ marked with A_1 in Fig. 3(d). (b), (c) Magnifications of the rectangles marked in (a), showing that the intervals $[c^1_{\mathcal{R}}, c^2_{\mathcal{R}}]$ and $[c^2_{\mathcal{L}}, c^1_{\mathcal{L}}]$ are invariant and absorbing. (d) Function $f^{m/2}$ at the parameter value $\mathit{\Gamma} = 5.8255$ marked with B_1 in Fig. 3(d). (e) Magnification of the rectangle marked in (d). The spikes are located outside the interval $[c^3_{\mathcal{R}}, c^2_{\mathcal{R}}]$. (f) Function $f^{m/2}$ at the parameter value $\mathit{\Gamma} = 5.8258$ marked with C_1 in Fig. 3(d). (g) Magnification of the rectangle marked in (f). Spikes, growing with increasing $\mathit{\Gamma}$, approach the unstable fixed point x^{**}. (h), (i) The same region as in (g) at the parameter values $\mathit{\Gamma} = 5.825837$ which corresponds to the final bifurcation and $\mathit{\Gamma} = 5.82588$ (after this bifurcation) which is marked with D_1 in Fig. 3(d).

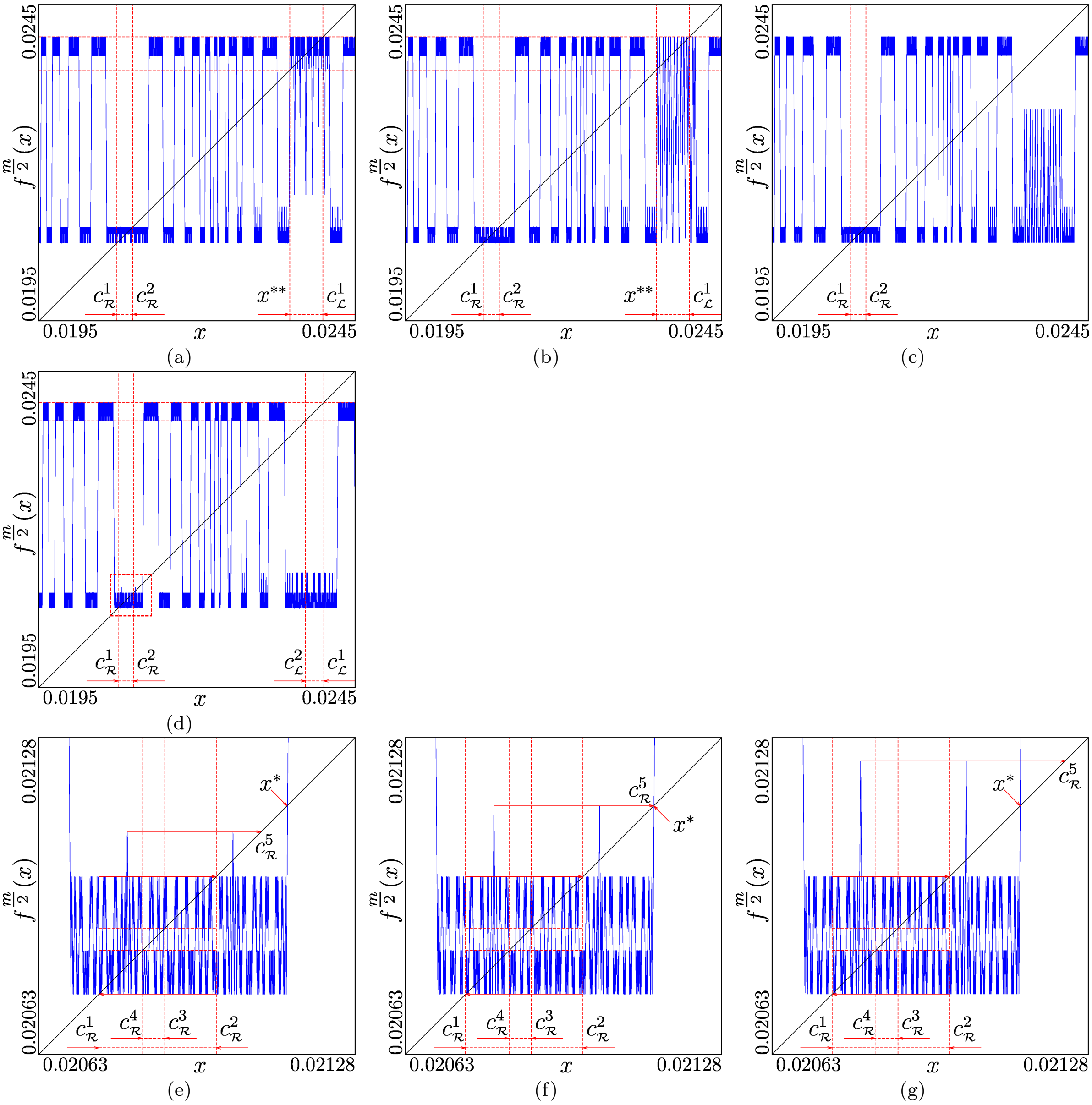

Fig. 5 (a), (b), (c) Function $f^{m/2}$ at the parameter values $\mathit{\Gamma} = 5.827$, $\mathit{\Gamma} = 5.828$, $\mathit{\Gamma} = 5.829$, respectively. With increasing $\mathit{\Gamma}$, the branches of the function, previously located in the interval $[c^2_{\mathcal{L}}, c^1_{\mathcal{L}}]$ move downwards and cease to intersect the diagonal. (d) Function $f^{m/2}$ at the parameter value $\mathit{\Gamma} = 5.8354$ marked with A_2 in Fig. 3(e). (e) Magnification of the rectangle marked in (d). The spikes start to grow in the interval $[c^1_{\mathcal{R}}, c^2_{\mathcal{R}}]$ and approach the fixed point x^*. (e), (f) The same region as in (d) at the parameter values $\mathit{\Gamma} = 5.835437$ which corresponds to the expansion bifurcation and $\mathit{\Gamma} = 5.8366$ (after this bifurcation) marked with B_2 in Fig. 3(e).

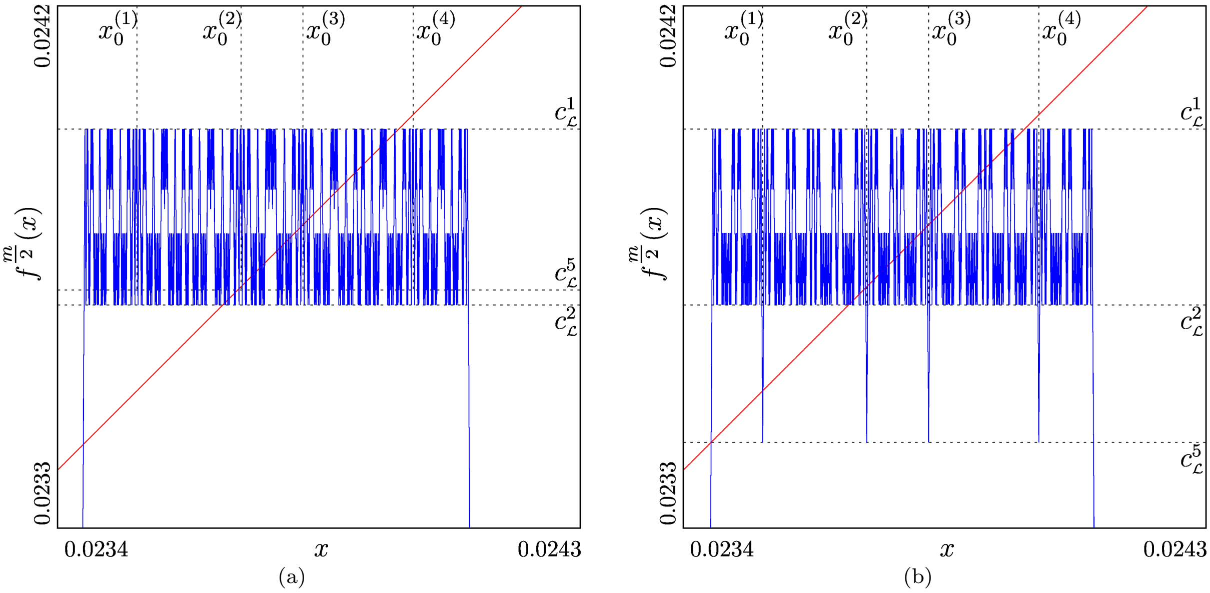

Fig. 6 Appearance of spikes. (a) $\Gamma = 5.8256$, there are no spikes. (b) $\Gamma = 5.825837$, there are four spikes with the tip points at $x^{(j)}$, $j = 1, 2, 3, 4$.

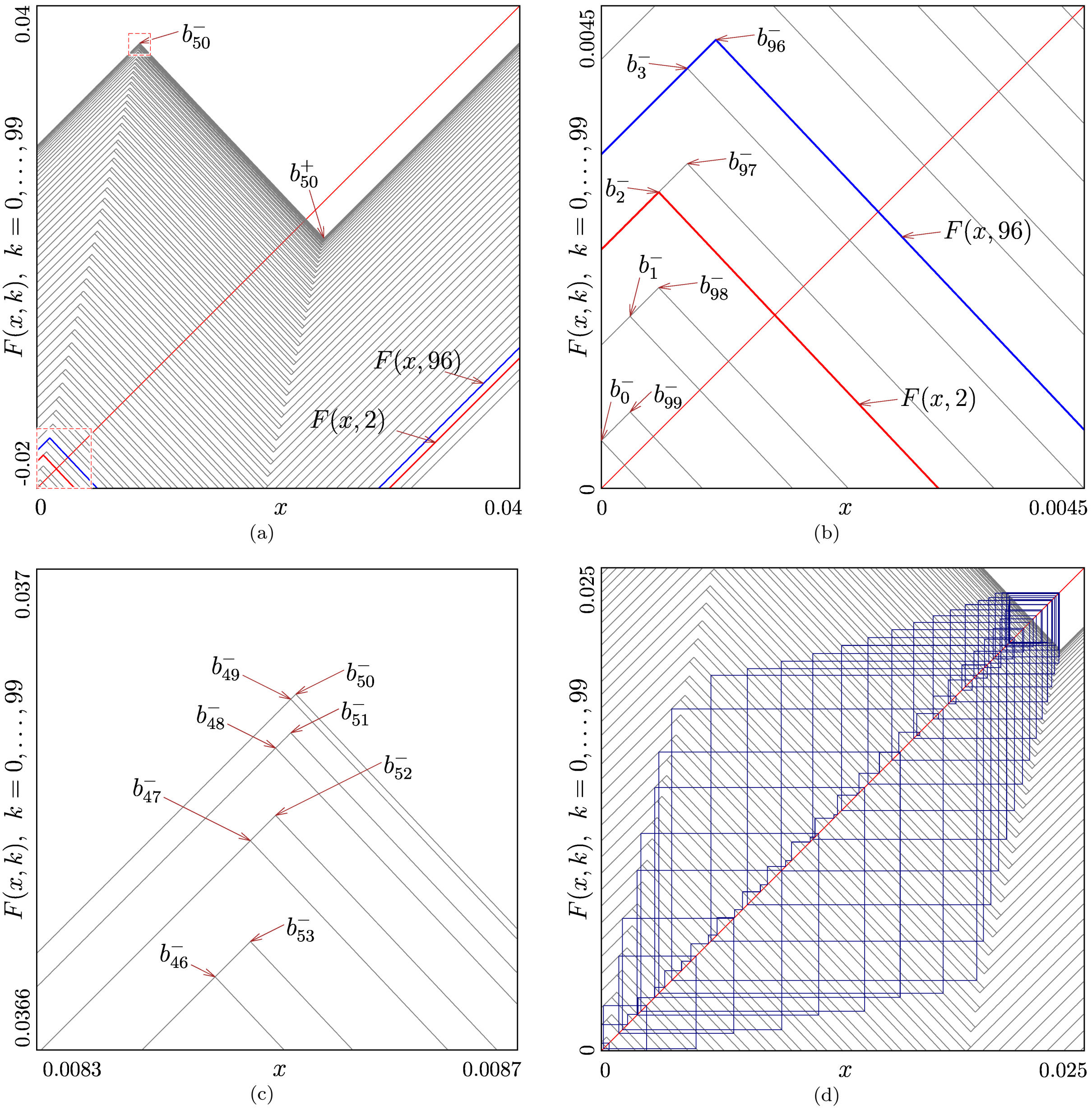

Fig. 7 (a) Functions $F_k(x)$ for fixed values of k, $0 \leqslant k < \frac{1}{2}m$. (b), (c) Magnifications of the rectangles marked in (a). For some k, the boundary points b_k^- and b_k^+ are marked. Additionally, the functions $F(x, 2)$ and $F(x, 96)$ are indicated. (d) Cobweb diagram of an unstable $\frac{1}{2}m$-cycle of map F. $\Gamma = 5.825837$.

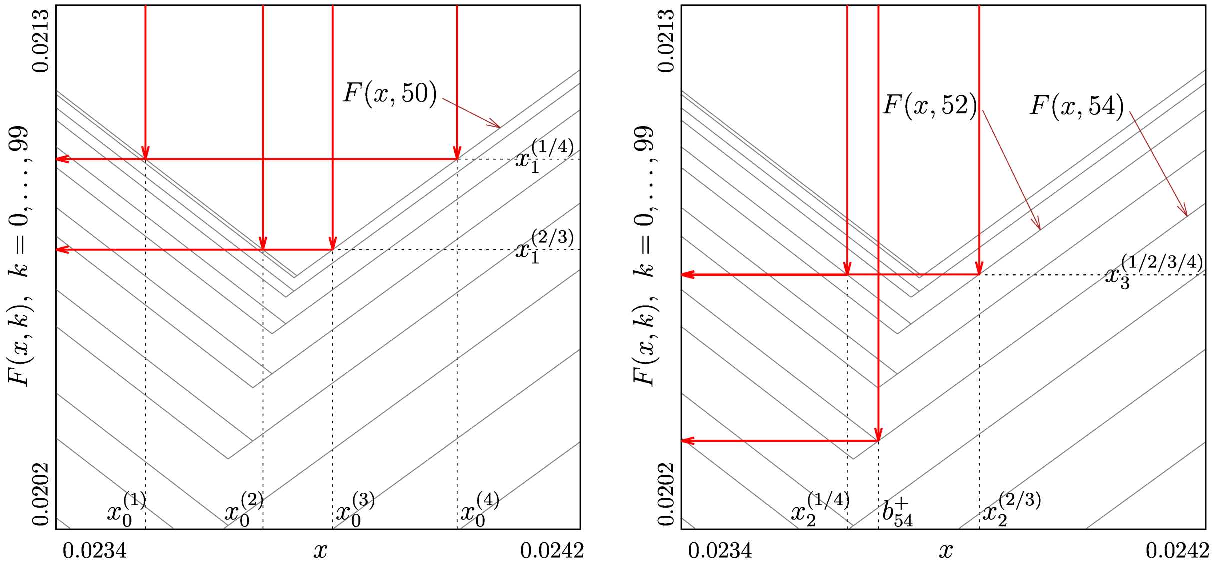

(a) (b)

Fig. 8 Developments of orbits started at the points $x_0^{(j)}$, $j = 1, 2, 3, 4$, corresponding to the tips of four spikes of $f^{m/2}$ shown in Fig. 6. (a) In the first step, the orbits merge pairwise, being mapped by the function $F(x, 50)$. (b) In the third step, the resulting two orbits are merged by the function $F(x, 50)$. Eventually, the resulting single orbit is mapped on the border point b_{54}^{+} of the function $F(x, 54)$. $\Gamma = 5.825837$.

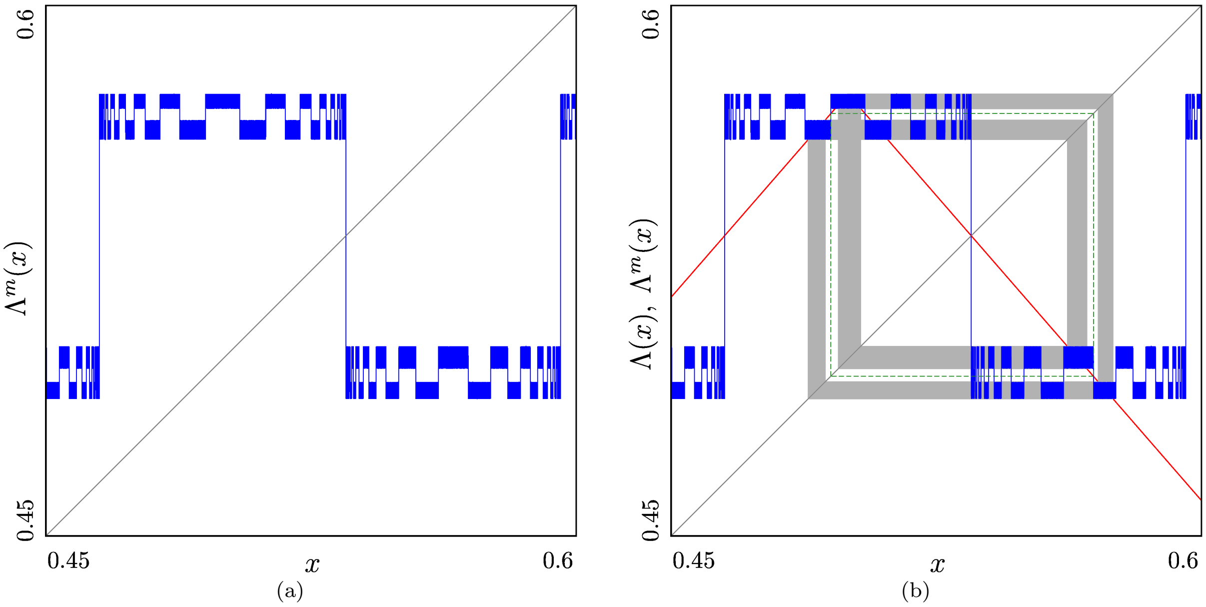

(a)

(b)

Fig. 9 (a) The function Λ^m for $\alpha = 1.15$ and $m = 100$. (b) in addition, the 4-band chaotic attractor of map T is shown. The long-range almost vertical branches intersecting the diagonal correspond to the repelling fixed point and the repelling 2-cycle of the tent map, the other (short-range) branches correspond to the 4-band chaotic attractor.

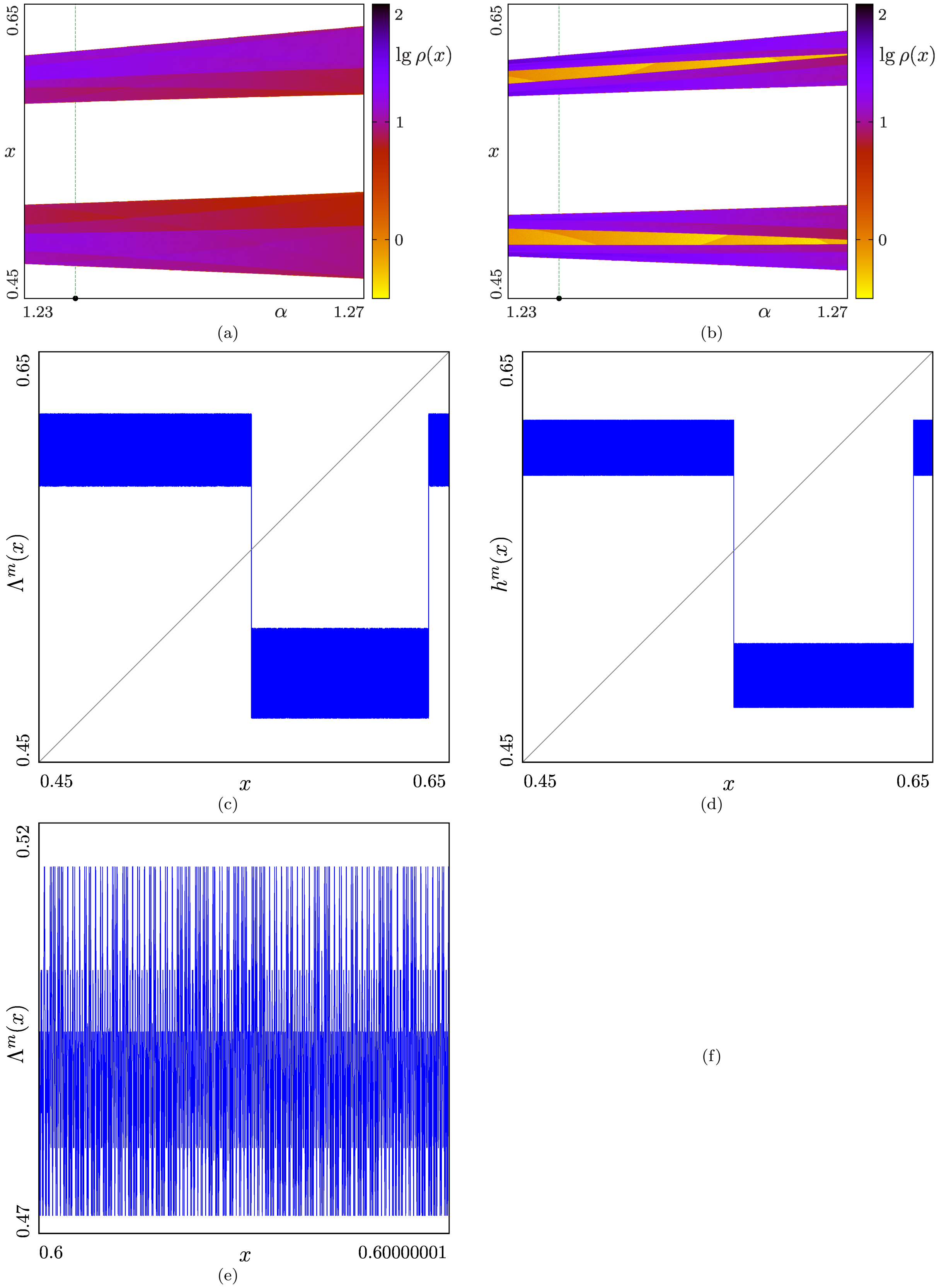

Fig. 10 Left column: original tent map (8); right column: non-autonomous tent map (9), $\beta = 0.1$, $m = 101$. (a) and (b): bifurcation diagrams showing the invariant density of the attractors. (c) and (d): function Λ^m and h^m at $\alpha = 1.236$ (the parameter value is indicated in (a) and (b)). (e) and (f): magnification of a small interval from (c) and (d). FIGURE 10(f) missing!